

## HYDRODYNAMIC MODELING OF ns-LASER ABLATION

DAVID AUTRIQUE, VASILIOS ALEXIADES, HARIHAR KHANAL

ABSTRACT. Laser ablation is a versatile and widespread technique, applied in an increasing number of medical, industrial and analytical applications. A hydrodynamic multiphase model describing nanosecond-laser ablation (ns-LA) is outlined. The model accounts for target heating and mass removal mechanisms as well as plume expansion and plasma formation. A copper target is placed in an ambient environment consisting of helium and irradiated by a nanosecond-laser pulse. The effect of variable laser settings on the ablation process is explored in 1-D numerical simulations.

### 1. INTRODUCTION

Due to its high spatial and temporal coherence, the laser is an excellent tool for precise material processing. The locally deposited laser energy can be used to remove material from the irradiated sample. This technique, known as laser ablation, is nowadays used in an increasing number of medical, industrial as well as analytical applications such as surgery, ophthalmology, nanoparticle manufacturing, pulsed laser deposition and micromachining, among many others [11, 16, 35, 36]. In certain industrial applications such as pulsed laser deposition [16] or analytical applications such as “nanosecond laser ablation inductively coupled plasma mass spectrometry” (ns-LA-ICP-MS), the ablation process takes place inside a chamber filled with an inert gas [36]. In case of LA-ICP-MS for instance, this ambient gas will transport the ablated matter through a tubing system towards the analysis equipment [36]. This experimental situation will be studied in the present work, with copper (Cu) being the target material and helium (He) the ambient gas.

It should be stressed that laser ablation results in a cascade of tightly coupled processes which depend on the laser parameters, sample characteristics as well as on the ambient environment. In a first step the target material will heat up, melt, evaporate and start to expand into the ambient environment. Subsequently the laser will trigger breakdown in the expanding vapor; the plume will partially ionize and a hot plasma is created above the sample surface. Since this plasma can absorb a significant amount of laser light, it will shield the target from the incoming laser beam and therefore reduce the amount of laser energy deposited in the sample. Such back-coupling effects render the experimental identification

---

2000 *Mathematics Subject Classification.* 92C45, 35K60, 65M99.

*Key words and phrases.* nanosecond laser ablation, hydrodynamic model, multiphase, plasma.

©2013 Texas State University - San Marcos.

Published ??.

of the mechanisms underlying laser ablation problematic. Therefore modeling and simulation are useful, as they allow a separate study of the intricately coupled processes.

*Nanosecond* laser ablation has been investigated by means of kinetic [27, 25, 19]; hydrodynamic [42, 1, 23, 29, 10, 6, 12, 39, 47, 34, 2, 18, 4, 8, 9]; as well as hybrid models such as [21, 24].

Because kinetic and hybrid models require long calculation times, one tries to employ hydrodynamic modeling if at all possible. Note that a macroscopic description of laser-material removal should treat the response of the material to variable pressure, energy and density. Therefore a multiphase approach is required [6, 39, 9] that accounts for the physical mechanisms in as well as above the irradiated target. Hence a hydrocode should account for target heating and the various ablation mechanisms as well as plume expansion and plasma formation.

In this paper we outline such a multiphase hydrodynamic model and present results of hydrodynamic simulations exploring the effect of variable laser wavelength and irradiance. In §2 we briefly describe some issues that arise during the modeling of nanosecond laser ablation. In §3 we outline some aspects of the hydrodynamic model that addresses these issues. In §4, 1-D hydrodynamic simulations for ns-laser ablation of a copper target (Cu) in a background gas (He), are presented. Calculations were done for a 6 ns laser pulse, operating in the UV-VIS regime at wavelengths of 266 nm and 532 nm, respectively and at laser fluences up to 10 J/cm<sup>2</sup>. Final conclusions are given in §5.

## 2. NANOSECOND LASER ABLATION

During and after the laser-material interaction, a complex cascade of tightly connected processes occurs in the vicinity of the target surface. As the copper sample heats up during ns-laser irradiation, a thin layer of material melts and finally vaporizes. At near-critical temperatures, the surface region of the material can arrive in a metastable liquid state. Here, homogeneous nucleation results in the formation of bubbles in the hot melt: the material will thermally fragment and decompose into a mixture consisting of vapor and liquid. As soon as the target material arrives in a (super)critical state, it experiences a liquid-plasma transition [32, 14]. The laser will trigger breakdown in the ablated material and a plasma starts to form. This plasma will absorb a part of the incoming laser light, and therefore shield the target from the laser beam. In the present work, laser induced absorption due to single and multi-photon ionization and inverse Bremsstrahlung are considered [40, 48] (see also section §3.2).

Due to these absorption mechanisms, a hot and quickly expanding plume is formed. The plasma pressure will increase and exceed the surface pressure of the material. Under such conditions the phase transition at the surface reverses and the material condenses back on the sample surface. Moreover the plasma pressure acting on the molten material can result in melt expulsion: molten material moves out of the irradiated material volume [5, 45]. At later times, typically several microseconds after the laser pulse, small particles are formed during the cooling stage of the plasma. Here homogeneous nucleation and recondensation processes in the plume result in the generation of nanosized droplets [20, 44]. In order to describe such a variety of processes, an effective hydrodynamic model should possess the following features:

- describe laser heating and account for the various ablation mechanisms,
- account for variable thermophysical and optical properties,
- treat plume expansion in an ambient environment,
- deal with plasma formation under non-equilibrium conditions,
- capture strong shocks via high resolution numerical schemes,
- be applicable in 1D, 2D as well as 3D.

Additional challenges in laser ablation modeling arise from:

- extreme space and time scales,
- extreme variation in material properties,
- the need for extensive datasets,
- the need for a wide-range multiphase equation of state.

In the next section, we outline some aspects of such a hydrodynamic model. For simplicity, and consistency with the 1-D numerical results, we present a 1-D version of the corresponding equations.

### 3. MULTIPHASE HYDRODYNAMIC MODEL

**3.1. Target.** In modeling ns-laser ablation, one can assume that the laser energy absorbed by the electrons is instantaneously redistributed and passed to the lattice. The electron and lattice subsystems of the target achieved thermal equilibrium; therefore target heating can be described by an ordinary heat conduction equation. Because material is removed (ablated) from the target, its surface will move with a certain recession velocity  $v_{\text{rec}}$ . Hence, it is computationally convenient to apply a Lagrangian formulation; target heating is described in a reference frame attached to the receding surface [9]:

$$\frac{\partial U}{\partial t} - v_{\text{rec}}(t) \frac{\partial U}{\partial x} = \frac{\partial}{\partial x} k(T) \frac{\partial T}{\partial x} + S_{\text{las}}(x, t). \quad (3.1)$$

In (3.1),  $U$  denotes the internal energy density,  $v_{\text{rec}}$  is the surface recession velocity, and  $k(T)$  represents the temperature dependent thermal conductivity [22]. The laser source term  $S_{\text{las}}$ , at position  $x$  and time  $t$ , is given by:

$$S_{\text{las}}(x, t) = I_a(t) (1 - R) \alpha e^{-\alpha x}. \quad (3.2)$$

Here  $R(T)$  and  $\alpha(T)$  denote the reflection and absorption coefficients of the target, respectively. They are calculated by fitting dielectric functions that account for intraband as well as interband transitions [7] to tabulated data [38]. The laser intensity (irradiance) at the target surface,  $I_a(t)$  is assumed to follow a Gaussian temporal profile with with standard deviation  $\sigma$ :

$$I_a(t) = \beta I_{\text{max}} e^{-(t-t_{\text{max}})^2/2\sigma^2}. \quad (3.3)$$

In (3.3),  $I_{\text{max}}$  denotes the maximum intensity (input parameter, see §4), whereas  $\beta$  represents the total shielding coefficient at the target surface that depends on the laser wavelength, plume temperature as well as on the species densities (neutrals, ions and electrons) above the target.

At all times the laser-heated material tends to adjust its pressure  $P_m$  to the ambient pressure  $P_{\text{amb}}$ . Pressure relaxation can be expressed as follows:

$$\frac{\partial P_m}{\partial t} - v_{\text{rec}}(t) \frac{\partial P_m}{\partial x} = -\frac{P_m - P_{\text{amb}}}{\tau_{\text{mech}}(x, t)}. \quad (3.4)$$

In (3.4),  $\tau_{\text{mech}}$  expresses the mechanical relaxation time; i.e. the time needed for a pressure wave to reach the target surface. Hence, one obtains  $\tau_{\text{mech}}(x, t) = x/c_{\text{snd}}(x, t)$ , where  $x$  and  $c_{\text{snd}}$  are the spatial coordinate and the local speed of sound in the target. For metals, the minimum mechanical relaxation time is typically in the order of 10 ps [15]. Since the target material will expand or compress locally after pressure relaxation, the density changes. Hence, the corresponding material velocity  $v(x, t)$  can be obtained from the continuity equation for  $\rho$ :

$$\frac{\partial \rho}{\partial t} - v_{\text{rec}}(t) \frac{\partial \rho}{\partial x} = - \frac{\partial \rho v}{\partial x} . \quad (3.5)$$

Mass and energy conservation, Eq.(3.1), (3.5), are valid mathematically, in weak sense, irrespective of the material phase [3]. At each timestep, the internal energy density  $U$ , material pressure  $P_m$ , mass density  $\rho$ , and material velocity  $v$  are updated to new time. In a next step, the corresponding phase state and material temperature are found. The system of equations (3.1)-(3.5) is closed by a multi-phase equation of state (EOS) [31]. A projection of the equation of state on the  $\rho - T$  plane is shown in Figure 1.

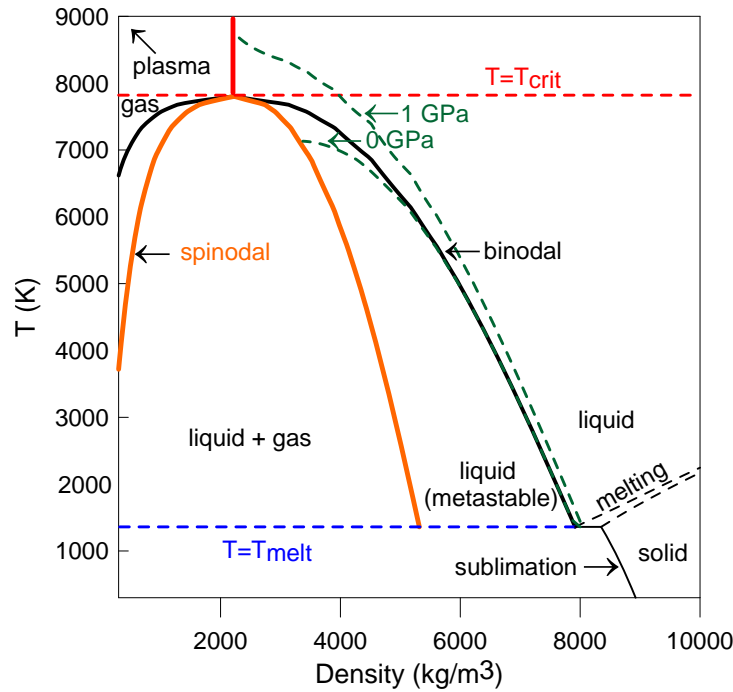


FIGURE 1. Phase diagram of copper projected on the  $\rho - T$  plane. In addition to the stable material phases (solid, liquid, gas and plasma), the metastable liquid and 2-phase (liquid+gas) regions, are represented. The respective phase boundaries (binodal, spinodal, melting and sublimation curves) are indicated. In addition, two isobars are shown that correspond to the minimum (0 GPa) and maximum pressures (1 GPa) encountered during the simulations.

Note that the recession velocity  $v_{\text{rec}}$  is one of the unknowns in the problem. In our model, three ablation mechanisms and corresponding recession velocities are distinguished, which are found as part of the numerical solution: (1) surface ablation due to evaporation and condensation,  $v_{\text{ev}}$ ; (2) volumetric mass removal due to bubble formation in the metastable state,  $v_{\text{bub}}$ ; and (3) volumetric ablation in the (super)critical region,  $v_{\text{crit}}$ . The recession velocity  $v_{\text{rec}}$  in (3.1) can therefore be formulated as [9]:

$$v_{\text{rec}}(t) = v_{\text{ev}}(t) + v_{\text{bub}}(t) + v_{\text{crit}}(t). \quad (3.6)$$

Hence (3.6) will depend on the material state and accordingly on the material temperature, pressure and density.

**3.2. Plume and Plasma.** The ablation mechanisms result in the creation of a dense plume that expands above the copper surface in the ambient gas, here helium. The expanding plume is modeled by a set of Euler equations:

$$\frac{\partial \rho}{\partial t} = -\frac{\partial \rho v}{\partial x}, \quad (3.7)$$

$$\frac{\partial \rho_v}{\partial t} = -\frac{\partial \rho_v v}{\partial x}, \quad (3.8)$$

$$\frac{\partial \rho v}{\partial t} = -\frac{\partial \rho v^2 + P}{\partial x}, \quad (3.9)$$

$$\frac{\partial \rho \varepsilon}{\partial t} = -\frac{\partial (\rho \varepsilon + P) v}{\partial x} - \frac{\partial q}{\partial x} + S_{\text{IB}} + S_{\text{PI}} - S_{\text{RAD}}. \quad (3.10)$$

These equations express mass (3.7), momentum (3.9) and energy conservation (3.10) in the plume domain. Here  $\rho = \rho_v + \rho_b$  denotes the total mass density, with  $\rho_v$  and  $\rho_b$  the partial densities of vapor and background gas, respectively. The total momentum density and the total energy density of plasma are  $\rho v$  and  $\rho \varepsilon$  respectively.  $P$  denotes the total pressure, whereas  $q$  is the heat flux transported by the various species in the plasma. In calculating  $q$ , an expression for the thermal conductivity is applied, which accounts for degeneracy as well as ionization effects [30]. The resulting numerical heat fluxes are limited using physical heat flux limiters, i.e. particles cannot move faster than their thermal velocity.

Note that species diffusion in the plume is not considered here due to the disparate time scales of the phenomena; diffusion processes become important much later, at near- $\mu\text{s}$  times [29].

The laser will trigger breakdown in the dense expanding vapor formed above the target surface. Laser induced breakdown is modeled by a collisional radiative model, presented in the accompanying article by Khanal et.al. [26]. The collisional radiative model accounts for the various collisional and radiative processes in the plasma, such as one-, two- and three-photon ionization, radiative decay, electron impact excitation and ionization, as well as the respective recombination reactions [17, 33, 37]. It describes the initial non-equilibrium state encountered in the plasma during the laser pulse. A set of rate equations (described in [26]) expresses the temporal evolution of the electron density and temperature, as well as the atomic level populations in the expanding plume. The equations account for the various collisional and radiative processes in the plasma. Since the species densities will drop quickly during the expansion process, it is reasonable to describe the plasma in the ideal gas approximation. Hence, the closure relations for the plasma are provided by the ideal gas equation of state.

The collisional radiative model provides the three source terms encountered in the energy equation (3.10). Here  $S_{\text{IB}}$  and  $S_{\text{PI}}$  are the energy source terms due to inverse Bremsstrahlung (IB) and one-, two-, and three-photon ionization (PI), respectively, whereas  $S_{\text{RAD}}$  is the radiation loss of the plasma [48].

After the breakdown stage, the collisional radiative model indicates that the (spatially averaged) plasma attains about equal electron, excitation, and heavy species temperatures, which means it approaches a state close to Local Thermodynamic Equilibrium (LTE). When the plume reaches a state close to LTE, the rate equations are switched off. Under LTE, the atomic levels become Boltzmann distributed and a local state is achieved where electrons, ions as well as the excited states are characterized by the same temperature  $T$ . At that instant the plasma is described in the ideal gas approximation and the temperature, electron and ion densities are retrieved from the Saha-Eggert equations [48]:

$$\frac{n_e x_i}{x_{i-1}} = \frac{u_i(T)}{u_{i-1}(T)} \left( \frac{2\pi m_e kT}{h^2} \right)^{\frac{3}{2}} \exp \left( -\frac{I_i}{kT} \right). \quad (3.11)$$

Here  $n_e$  denotes the total electron number density,  $x_i$   $x_{i-1}$  are the molar fractions of ions at states  $i$  and  $i-1$ , respectively,  $m_e$  is mass of electron,  $k$  is the Boltzmann constant,  $h$  is the Planck constant.  $I_i$  is the ionization potential of the ion with respect to state  $i-1$ ,  $u_i(T)$  is the electronic partition function for an ion in state  $i$  [41]. The Saha equations and corresponding closure relations are solved iteratively by a Newton-Raphson method to calculate the unknowns  $n_e$ ,  $x_i$  and  $T$ .

**3.3. Computational Strategy.** The target is discretized into a non-uniform grid, with high nodal density near the surface. The smallest target cells (of size 6 nm) are placed in the near-surface region. They resolve the absorption length  $1/\alpha(T)$  over which laser energy is deposited (see (3.2)). Initially, the plume region is discretized into a uniform grid of length  $\Delta x = 500$  nm. Adaptive mesh refinement is used to resolve the strong gradients encountered in the plume domain [43]. The mesh in the plume domain is refined till the grid reaches a lower limit of 50 nm. Moreover, the grid expands ahead of the heat wave in the target domain and ahead of the expanding plasma in the plume domain.

A central second order advection scheme is applied [28], while the temporal evolution of the problem proceeds through explicit time-stepping (see the accompanying article [26]). Variable time-stepping is employed respecting the CFL condition in the entire computational domain. Time steps are of order  $10^{-13}$  s. The total simulation time is 50 ns, well beyond the duration of a single laser pulse.

#### 4. NUMERICAL SIMULATIONS

We present 1-D simulations of laser ablation of copper (Cu) in a background gas (He) under variable laser settings. The copper target and the background gas reside initially in a stationary state and are initialized at standard pressure and temperature (STP). The entire system (target+background gas) is irradiated by a ns-laser pulse of 6 ns FWHM (Full Width at Half Maximum). The laser operates in the UV-VIS regime at wavelengths of 266 nm or 532 nm and at variable irradiances ( $4 \times 10^{12}$  -  $1.6 \times 10^{13}$  W/m<sup>2</sup>). The employed irradiances, correspond to fluences that vary between 2 and 10 J/cm<sup>2</sup>. In the following sections, numerical simulations are shown that represent the evolution of the target and plasma plume for the laser settings mentioned above. In §4.1-4.3, results are presented for laser pulses

operating at variable wavelengths and fixed maximum peak irradiances of  $10^{13}$  W/m<sup>2</sup>, whereas in §4.4 a full parametric study is employed for the calculation of plasma transmissivities and ablation depths.

**4.1. Target Heating.** The temporal evolution of the surface temperature and laser intensities (irradiances) at the target surface are depicted in Fig.2(a). Two laser pulses with a peak irradiance of  $10^{13}$  W/m<sup>2</sup> (black curve) interact with the copper surface. The first laser pulse operates in the ultraviolet region, at 266 nm, whereas the second produces visible, monochromatic light at 532 nm. During the laser-material interaction the copper target will heat up very fast. Around 7 ns the surface temperature exceeds the normal boiling point ( $T_{\text{boil}} = 2836$  K) and evaporation becomes significant. At that instant, a plume consisting of evaporated copper develops above the target surface. After 8 ns, the material reaches near-critical temperatures ( $T_{\text{crit}} = 7800$  K) Now the material arrives in a metastable state near the binodal (not shown here) and will fragment thermally. A lot of material enters the plume domain in a short time and starts to expand above the surface. The laser triggers breakdown of the material in the dense plume and a plasma is formed above the surface. The plasma will shield the target from the laser and reduce the laser intensity at the surface. The actual intensities at the target surface are shown for 266 nm (blue curve) and 532 nm (red curve), respectively, which clearly exhibits a decreasing trend of temperature and intensity at the surface after 8 ns.

However, since the laser light still reaches the target surface, the heating process proceeds; around 9 ns the copper target arrives in the supercritical state. The target experiences a liquid-plasma transition and material is ejected in the plume domain. The mass density near the target surface increases, whereas the plasma responds through laser absorption and subsequent expansion; as a result oscillations are observed in the laser irradiance patterns as seen in Fig.2(a). Fig.2(b) depicts time dependent profiles of the reflectivities and the surface temperature for both cases. Since the material will expand during the laser heating, its electron density decreases and the reflectivity starts to drop. Around 10 ns, the material arrives in a supercritical state; the strong reduction of the electron density results in a drastic change of the optical properties; the hot melt near the surface becomes quasi-transparent. At the end of the laser pulse, the situation is reversed: the surface temperature decreases and the reflectivity increases again. Although the initial reflectivity of the copper target, irradiated by a 266 nm pulse is half the value of the reflectivity in the 532 case, similar minima are encountered around 10 ns. Hence, the amount of laser energy reaching the target is similar in both cases (see (3.2)) and the target properties behave alike for both laser wavelengths.

**4.2. Plasma Formation.** The onset of laser induced breakdown is modelled by a collisional radiative model (see §3.2); computational details can be found in the article of Khanal et.al. [26]. During the laser action, photon ionization (PI) triggers breakdown of the gaseous copper in the vapor above the target surface. As a result, a significant amount of ions and electrons is formed in the expanding plume. The electrons will speed up in the laser field and collide with the present neutrals and ions; at this stage the laser-plasma absorption proceeds through Inverse Bremsstrahlung (IB). Figures 3(a-b) represent temporal profiles for spatial averaged absorption coefficients at wavelengths of 266 and 532 nm, respectively. The laser

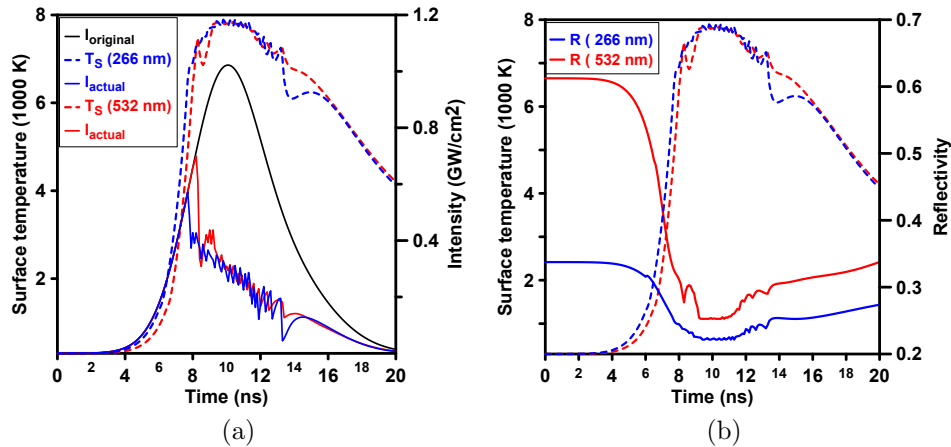


FIGURE 2. Dashed curves represent surface temperature for  $\lambda = 266$  nm (blue) and for  $\lambda = 532$  nm (red). The peak irradiance is the same in both cases ( $I_{\text{max}} = 10^{13}$  W/m<sup>2</sup>). Solid curves depict: (a) laser intensity: original intensity (black) and actual intensities for  $\lambda = 266$  nm (blue) and for  $\lambda = 532$  nm (red). (b) reflectivity: for  $\lambda = 266$  nm (blue) and for  $\lambda = 532$  nm (red).

pulse duration and intensity are the same in both cases (FWHM=6 ns,  $I_{\text{max}} = 10^{13}$  W/m<sup>2</sup>). Although the total absorption coefficient ( $\alpha_{\text{TOTAL}}$ ), attains similar values in both cases, the absorption coefficients of the underlying processes ( $\alpha_{\text{PI}}$  and  $\alpha_{\text{IB}}$ ), are clearly different. In case of 266 nm laser irradiation (see Fig.3(a)),  $\alpha_{\text{MPI}}$  dominates during the entire time. In the 532 nm case, however, Inverse Bremsstrahlung due to electron-ion collisions ( $\alpha_{\text{IB}}$ ), dominates after 9.5 ns (see brown solid line in Fig.3(b)). This effect can be attributed to the fact that the efficiency of (multi) photon ionization absorption increases at decreasing wavelengths ( $\sim 1/\lambda$ ), whereas the absorption coefficients for electron-ion Inverse Bremsstrahlung scale as the cube of the laser wavelength ( $\sim \lambda^3$ ). Since the total absorption coefficients are similar, the total amount of energy invested in the plasma will be about the same. Therefore, the overall behavior of the plasma will be similar as well. This observation indicates that one has to be careful with the interpretation of experimental data in such a situation; although similar plasma behavior would be observed here, the underlying absorption mechanisms are clearly different.

**4.3. Plume Expansion.** During the ablation process a lot of ablated copper enters the plume domain and a high density region near the target surface is formed (Fig.4(a)). The dense plume will expand above the surface, while it pushes the ambient helium gas away (see Fig.4(b)). Both the ablated material and the background gas pile up near their interface. This effect is known as the “snowplow effect” [24]. Laser induced breakdown results in a hot plasma (Fig.5(a)) that expands at speeds in the order of 10 km/s above the target surface (Fig.5(b)). Since the plume pressure above the target surface increases, a situation is encountered where the plume pressure exceeds the pressure at the target surface. Hence material moves back towards the target and condenses on the surface. This results in negative velocities in the vicinity of the target (Fig.5(b)). After the end of the laser

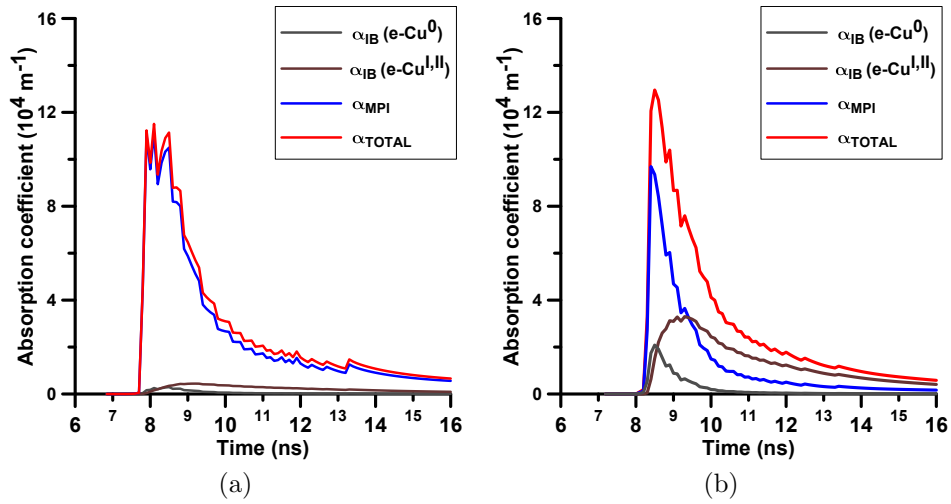


FIGURE 3. Time evolution of spatially averaged absorption coefficients in the plasma is shown for the same peak irradiance ( $I_{max} = 10^{13} \text{ W/m}^2$ ). Solid lines represent absorption due to photo-ionization ( $\alpha_{MPI}$ ), electron-neutral and electron-ion inverse Bremsstrahlung ( $\alpha_{IB}$ ) as well as the total absorption coefficient ( $\alpha_{TOTAL}$ ): (a) for  $\lambda = 266 \text{ nm}$  (b) for  $\lambda = 532 \text{ nm}$

pulse, here around 16 ns, the temperature and velocity will decrease as the plasma expands (see Fig.5(a-b)).

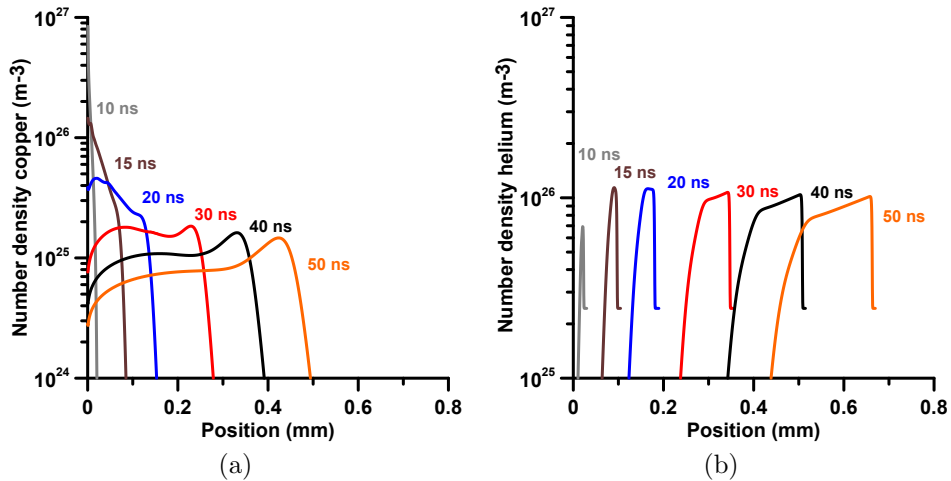


FIGURE 4. Spatial profiles of species number densities at different times for the same laser settings as in Fig.3. Since the results for 266 and 532 nm are very similar, only the case  $\lambda = 266 \text{ nm}$  is shown. (a) number density of ablated material (copper); (b) number density of background gas (helium).

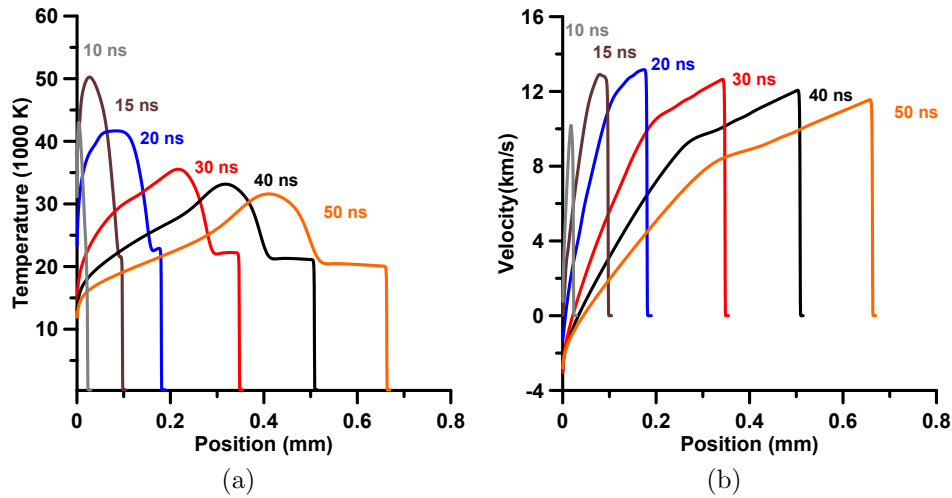


FIGURE 5. Spatial temperature (a) and velocity (b) profiles at various times, for 266 nm laser pulse operating at peak irradiance  $10^{13}$  W/m<sup>2</sup>.

**4.4. Ablation depths and Transmission data.** Figures 6(a) and 6(b) show calculated ablated depths and transmissivities at two wavelengths and for fluences (i.e. integrated irradiances) up to 10 J/cm<sup>2</sup>. In the 266 nm case, higher ablated depths are found, when compared to the 532 nm case (see Fig.6(a)). Since the 266 nm laser will penetrate deeper into the target material, more material will be removed than in the 532 nm case (see 6(a)). The plasma formed above the surface will shield the laser from the target. Since the surface integrals of the total absorption coefficients are about the same for both wavelengths, more plasma shielding will occur in the situation where more “absorbers” (species) are encountered, here the 266 nm case. Thus, the transmissivities exhibit the opposite behavior, the 266 nm wavelength generates more plasma shielding than the 532 nm one.

Note that transmissivities represent the amount of laser energy that was distributed between plasma and target. In case the transmissivities would deviate from transmission experiments such as [46, 13, 18], it would mean that the model fails to predict correct energy balances in the domain and automatically implies that the underlying physics needs to be revised. Since mass removal is governed by a complex cascade of processes that occur in and above the target, comparison of calculated and measured ablation depths are an additional valuable step in the validation of the model. Experimental verification studies are planned in the near future.

## 5. CONCLUSION

A hydrodynamic multiphase model for laser ablation of copper in an ambient environment consisting of helium is presented. During laser irradiation, several complex, tightly coupled physical processes occur in and above the target. Surface as well as volumetric ablation mechanisms, result in the formation of a dense vapor plume above the surface. The laser triggers breakdown in the vapor and a hot, quickly expanding plasma is created above the target. The onset of laser induced

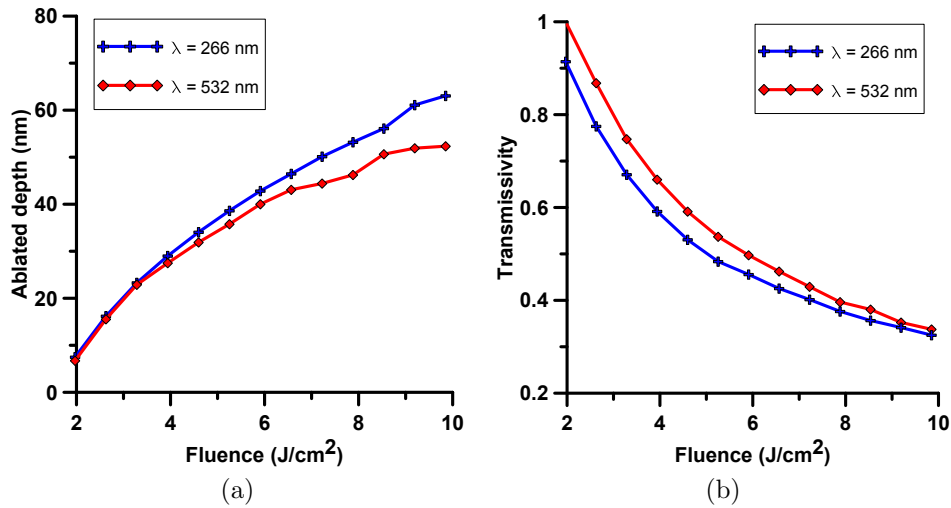


FIGURE 6. Transmission data and ablated depths for variable laser settings. Simulations were performed for a range of irradiances corresponding to fluences up to  $10 \text{ J/cm}^2$ . Results are for wavelengths 266 nm (blue) and 532 nm (red): (a) Ablated depths (b) Transmissivity

breakdown in the vapor is modelled, employing a collisional radiative model. As soon as a state close to Local Thermodynamic Equilibrium is achieved, the collisional radiative model is switched off and the plasma description proceeds through the solution of Saha-Eggert equations.

Numerical results show the evolution of the target and plasma plume at various laser settings. The laser operates in the UV-VIS regime at wavelengths of 266 nm or 532 nm, and at fluences up to  $10 \text{ J/cm}^2$ . Despite the fact that both wavelengths result in similar behavior of the target and plasma, it is found that the underlying absorption mechanisms in the plasma are different. Whereas photo-ionization dominates the entire absorption process in the case of 266 nm laser irradiation, Inverse Bremsstrahlung processes compete with photo-ionization under 532 nm irradiation. Although similar plasma behavior could be experimentally observed in such a case, the underlying mechanisms can clearly be different.

Our results indicate that the interpretation of experimental data in such a situation might be much more complicated than it would seem at first sight. Hence, both modeling and experimental verification are required for a detailed understanding of the mechanisms underlying ns-laser ablation.

**Acknowledgements.** The authors wish to thank P. Levashov, K. Khishenko and M. Povarnitsyn for the equation-of-state data set and advice. The first author (DA) acknowledges financial support from the Deutsche Forschungsgemeinschaft (Emmy Noether-Program, grant RE 1141/11).

## REFERENCES

1. M. Aden, E.W. Kreutz, and A Voss, *Laser-induced plasma formation during pulsed laser deposition*, Journal of Physics D: Applied Physics **26** (1993), 1545.
2. M. Aghaei, S. Mehrabian, and S.N. Tavassoli, *Simulation of nanosecond pulsed laser ablation of copper samples: A focus on laser induced plasma radiation*, Journal of Applied Physics **104** (2008), no. 5, 053303.
3. V. Alexiades, *Mathematical modeling of melting and freezing processes*, Hemisphere, 1992.
4. V. Alexiades and D. Autrique, *Enthalpy model for heating, melting, and vaporization in laser ablation*, Electronic Journal of Differential Equations **Conf. 19** (2010), 1–14.
5. M. Von Allmen and A. Blatter, *Laser-beam interactions with solid materials: Physical principles and applications, 2nd updated ed*, Springer Verlag, Berlin, 1995.
6. S.I. Anisimov and B.S. Luk'yanchuk, *Selected problems of laser ablation theory*, Physics-Usppekhi **45** (2002), 293.
7. NW Ashcroft and K Sturm, *Interband absorption and the optical properties of polyvalent metals*, Physical Review B **3** (1971), no. 6, 1898.
8. D. Autrique, Z. Chen, V. Alexiades, A. Bogaerts, and B. Rethfeld, *A multiphase model for pulsed ns-laser ablation of copper in an ambient gas*, AIP Conference Proceedings, vol. 1464, 2012, p. 648.
9. D. Autrique, G. Clair, D. L'Hermite, V. Alexiades, A. Bogaerts, and B. Rethfeld, *The role of mass removal mechanisms in the onset of ns-laser induced plasma formation*, Journal of Applied Physics **114** (2013), no. 2, 023301.
10. L. Balazs, R. Gijbels, and A Vertes, *Expansion of laser-generated plumes near the plasma ignition threshold*, Analytical Chemistry **63** (1991), no. 4, 314–320.
11. D. Bäuerle, *Laser processing and chemistry*, Springer Verlag, Berlin, 2011.
12. A.V. Bulgakov and N.M. Bulgakova, *Dynamics of laser-induced plume expansion into an ambient gas during film deposition*, Journal of Physics D: Applied Physics **28** (1995), no. 8, 1710–1718.
13. ———, *Thermal model of pulsed laser ablation under the conditions of formation and heating of a radiation-absorbing plasma*, Quantum Electronics **29** (1999), no. 5, 433–437.
14. N.M. Bulgakova and A.V. Bulgakov, *Pulsed laser ablation of solids: transition from normal vaporization to phase explosion*, Applied Physics A: Materials Science & Processing **73** (2001), no. 2, 199–208.
15. B. Chimier, V.T. Tikhonchuk, and L. Hallo, *Effect of pressure relaxation during the laser heating and electron-ion relaxation stages*, Applied Physics A: Materials Science & Processing **92** (2008), no. 4, 843–848.
16. D.B. Chrisey and G.K. Hubler, *Pulsed laser deposition of thin films*, Wiley, New York, 1994.
17. H.K. Chung, M.H. Chen, W.L. Morgan, Y. Ralchenko, and R.W. Lee, *Flychk: Generalized population kinetics and spectral model for rapid spectroscopic analysis for all elements*, High Energy Density Physics **1** (2005), no. 1, 3–12.
18. G. Clair and D. L'Hermite, *1D modelling of nanosecond laser ablation of copper samples in argon at  $P=1$  atm with a wavelength of 532 nm*, Journal of Applied Physics **110** (2011), no. 8, 083307.
19. F. Garrelie, C. Champeaux, and A. Catherinot, *Study by a monte carlo simulation of the influence of a background gas on the expansion dynamics of a laser-induced plasma plume*, Applied Physics A: Materials Science & Processing **69** (1999), no. 1, 45–50.
20. A.G. Gnedovets, A.V. Gusarov, and I. Smurov, *A model for nanoparticles synthesis by pulsed laser evaporation*, Journal of Physics D: Applied Physics **32** (1999), no. 17, 2162.
21. S.S. Harilal, C.V. Bindhu, M.S. Tillack, F. Najmabadi, and AC Gaeris, *Internal structure and expansion dynamics of laser ablation plumes into ambient gases*, Journal of Applied Physics **93** (2003), no. 5.
22. C.Y. Ho, R.W. Powell, and P.E. Liley, *Thermal conductivity of the elements*, Journal of Physical and Chemical Reference Data **1** (1972), 279.
23. J.R. Ho, C.P. Grigoropoulos, and J.A.C. Humphrey, *Computational study of heat transfer and gas dynamics in the pulsed laser evaporation of metals*, Journal of Applied Physics **78** (1995), no. 7, 4696.
24. T.E. Itina, J. Hermann, P. Delaporte, and M. Sentis, *Laser-generated plasma plume expansion: Combined continuous-microscopic modeling*, Physical Review E **66** (2002), no. 6, 1–12.

25. T.E. Itina, V.N. Tokarev, W. Marine, and M. Autric, *Monte Carlo simulation study of the effects of nonequilibrium chemical reactions during pulsed laser desorption*, Journal of Chemical Physics **106** (1997), no. 21, 8905.
26. H. Khanal, D. Autrique, and V Alexiades, *Time-stepping for laser ablation*, Electronic Journal of Differential equations, (in this volume) (2013).
27. J.C.S. Kools, *Monte carlo simulations of the transport of laser-ablated atoms in a diluted gas*, Journal of applied physics **74** (1993), no. 10, 6401–6406.
28. A. Kurganov and E. Tadmor, *New high-resolution central schemes for nonlinear conservation laws and convection–diffusion equations*, Journal of Computational Physics **160** (2000), no. 1, 241–282.
29. H.C. Le, D.E. Zeitoun, J.D. Parisse, M. Sentis, and W. Marine, *Modeling of gas dynamics for a laser-generated plasma: propagation into low-pressure gases*, Physical Review E **62** (2000), no. 3 Pt B, 4152–61.
30. Y.T. Lee and R.M. More, *An electron conductivity model for dense plasmas*, Physics of Fluids **27** (1984), no. 5, 1273.
31. P.R. Levashov and K.V. Khishchenko, *Itteos 5.8 software for calculation of eos for metals*, 2007.
32. A.A. Likalter, *Equation of state of metallic fluids near the critical point of phase transition*, Physical Review B: Condensed Matter and Materials Physics **53** (1996), no. 8, 4386.
33. V.I. Mazhukin, V.V. Nossov, M.G. Nikiforov, and I. Smurov, *Optical breakdown in aluminum vapor induced by ultraviolet laser radiation*, Journal of Applied Physics **93** (2003), 56.
34. V.I. Mazhukin, V.V. Nossov, and I. Smurov, *Modeling of plasma-controlled evaporation and surface condensation of Al induced by 1.06 and 0.248  $\mu$ m laser radiations*, Journal of Applied Physics **101** (2007), no. 2, 024922.
35. J.C. Miller and R.F. Haglund, *Laser ablation and desorption*, Academic Press, New York, 1998.
36. A. Montaser, *Inductively coupled plasma mass spectrometry*, Wiley, New York, 1998.
37. V. Morel, A. Bulte, and B.G. Chéron, *Modeling of thermal and chemical non-equilibrium in a laser-induced aluminum plasma by means of a collisional-radiative model*, Spectrochimica Acta, Part B: Atomic Spectroscopy **65** (2010), no. 9, 830–841.
38. E.D. Palik, *Handbook of optical constants of solids, vol. 1*, Academic Press, New York, 1997.
39. M.S. Qaisar and G.J. Pert, *Laser ablation of Mg, Cu, and Pb using infrared and ultraviolet low-fluence lasers*, Journal of Applied Physics **94** (2003), no. 3, 1468.
40. L.J. Radziemski and D.A. Cremers, *Laser-induced plasmas and applications*, vol. 21, ch. R.G.Root.-Modelling of Post-Breakdown Phenomena, pp. 9–103, Marcel Dekker, New York, 1989.
41. Y. Ralchenko, A.E. Kramida, J. Reader, and N.A.S.D. Team, *Nist atomic spectra database (version 3.1. 5)*, 2008.
42. R. Singh and J. Narayan, *Pulsed-laser evaporation technique for deposition of thin films: Physics and theoretical model*, Physical Review B **41** (1990), no. 13, 8843–8859.
43. M. Tang and T. Tang, *Adaptive mesh methods for one-and two-dimensional hyperbolic conservation laws*, SIAM Journal on Numerical Analysis **41** (2003), no. 2, 487–515.
44. M.S. Tillack, D.W. Blair, and S.S. Harilal, *The effect of ionization on cluster formation in laser ablation plumes*, Nanotechnology **15** (2004), no. 3, 390.
45. K.T. Voisey, S.S. Kudesia, W.S.O. Rodden, D.P. Hand, J.D.C Jones, and T.W. Clyne, *Melt ejection during laser drilling of metals*, Materials Science & Engineering, A: Structural Materials: Properties, Microstructure and Processing **356** (2003), no. 1-2, 414–424.
46. A.Y. Vorob'ev, *Reflection of pulsed ruby laser radiation by a copper target in air and in vacuum*, Soviet Journal of Quantum Electronics **15** (1985), no. 4, 490–493.
47. S.B. Wen, X. Mao, R. Greif, and R.E. Russo, *Expansion of the laser ablation vapor plume into a background gas. I. Analysis*, Journal of Applied Physics **101** (2007), no. 2, 023114.
48. B. Zel'dovich and Y.P. Raizer, *Physics of shock waves and high-temperature hydrodynamic phenomena*, vol. 1,2, Dover, New York, 2002.

DAVID AUTRIQUE

PHYSICS, OPTIMAS RESEARCH CENTER - TU KAISERSLAUTERN, 67653 KAISERSLAUTERN, GERMANY

VASILIOS ALEXIADES  
MATHEMATICS, UNIVERSITY OF TENNESSEE, KNOXVILLE, TN 37996, USA

HARIHAR KHANAL  
MATHEMATICS, EMBRY-RIDDLE AERONAUTICAL UNIVERSITY DAYTONA BEACH, FL 32114, USA